USER GUIDE
Planetary-Code-Collection:
Thermal and Ice Evolution Models
for Planetary Surfaces

Norbert Schörghofer (norbert@psi.edu)

Honolulu, Hawaii

2002–2019

Last updated September 20, 2019

Contents

2

Preface

Companion to https://github.com/nschorgh/Planetary-Code-Collection/

Technical Notes:
Most of the code was developed with a `gfortran` compiler on an Intel processor. Many components were also run on various Linux clusters, sometimes using other compilers. The non-portable `real(8)` is meant to correspond to an 8-byte floating point number.

Cite user guide or source code as:
N. Schörghofer. Planetary-Code-Collection: Thermal and Ice Evolution Models for Planetary Surfaces v1.1.5, 2017. GitHub. doi:10.5281/zenodo.594268
This doi points to the most recent release (currently 1.1.5), but not necessarily to the most recent version. The URL above points to the most recent version.

Part 1

Conduction of Heat: 1D Thermal Model for Planetary Surface

1-Dimensional Numerical Model of Thermal Conduction and Surface Energy Balance

Authors & History: originally implemented by Samar Khatiwala in 2001 (including upper radiation boundary condition for semi-implicit scheme); extended to variable thermal properties and irregular grid by Norbert Schörghofer 2002–2003

Governing equation for the surface energy balance:

$$\rho c \frac{\partial T}{\partial t} = \frac{\partial}{\partial z}\left(k\frac{\partial T}{\partial z}\right) \tag{1.1}$$

T ... temperature, t ... time, z ... depth, ρc ... volumetric heat capacity, k ... thermal conductivity
$F = k\frac{\partial T}{\partial z}$ ... heat flux
+ various boundary conditions specified below. Note that a radiation upper boundary condition is non-linear, and needs to be linearized for an implicit numerical solver.

1.1   Semi-Implicit Scheme on Irregular Grid

$$\frac{\partial}{\partial z}F_j = \frac{F_{j+\frac{1}{2}} - F_{j-\frac{1}{2}}}{(z_{j+1} - z_{j-1})/2} = 2\frac{k_{j+\frac{1}{2}}\frac{T_{j+1}-T_j}{z_{j+1}-z_j} - k_{j-\frac{1}{2}}\frac{T_j-T_{j-1}}{z_j-z_{j-1}}}{z_{j+1} - z_{j-1}}$$

$$(\rho c)_j \frac{\partial T_j}{\partial t} = \frac{2k_{j+\frac{1}{2}}}{(z_{j+1} - z_j)(z_{j+1} - z_{j-1})}T_{j+1} - \frac{2}{z_{j+1} - z_{j-1}}\left(\frac{k_{j+\frac{1}{2}}}{z_{j+1} - z_j} + \frac{k_{j-\frac{1}{2}}}{z_j - z_{j-1}}\right)T_j +$$

$$+ \frac{2k_{j-\frac{1}{2}}}{(z_j - z_{j-1})(z_{j+1} - z_{j-1})}T_{j-1}$$

$$\text{introduce}\quad \alpha_j = \frac{\Delta t}{(\rho c)_j}\frac{k_{j+\frac{1}{2}}}{(z_{j+1} - z_j)(z_{j+1} - z_{j-1})}\quad \text{and}\quad \gamma_j = \frac{\Delta t}{(\rho c)_j}\frac{k_{j-\frac{1}{2}}}{(z_j - z_{j-1})(z_{j+1} - z_{j-1})} \tag{1.2}$$

$$\Delta t\frac{\partial T_j}{\partial t} = 2\alpha_j T_{j+1} - 2(\alpha_j + \gamma_j)T_j + 2\gamma_j T_{j-1}$$

$$T_j^{n+1} - T_j^n = \alpha_j T_{j+1}^{n+1} - (\alpha_j + \gamma_j)T_j^{n+1} + \gamma_j T_{j-1}^{n+1} + \alpha_j T_{j+1}^n - (\alpha_j + \gamma_j)T_j^n + \gamma_j T_{j-1}^n$$

$$\boxed{-\alpha_j T_{j+1}^{n+1} + (1 + \alpha_j + \gamma_j)T_j^{n+1} - \gamma_j T_{j-1}^{n+1} = \alpha_j T_{j+1}^n + (1 - \alpha_j - \gamma_j)T_j^n + \gamma_j T_{j-1}^n} \quad 1 < j < N \quad (1.3)$$

Superscript n refers to the time step. Subscript j refers to position z_j. Whereas the temperature T_j is defined on grid point z_j, the conductivity k is defined on half-points. In the equations above, $(\rho c)_j$ is defined on z_j, but in the program implementations, $2(\rho c)_j = (\rho c)_{j+\frac{1}{2}} + (\rho c)_{j-\frac{1}{2}}$. In this way, the thermal properties k and ρc are defined on the same points and, in particular, they do not need to be defined at an interface of two layers with different thermal properties when that interface coincides with a grid point. Since array indices must be integers, we choose $k[j] = k_{j-\frac{1}{2}}$, and the same for ρc.

1.1.1 Upper boundary condition: radiation

$$Q + k \left.\frac{\partial T}{\partial z}\right|_{z=0} = \epsilon \sigma T^4 \big|_{z=0} \tag{1.4}$$

Q is the incoming solar flux including the atmospheric contribution.
introduce auxiliary quantity T_0, such that surface temperature $T_s = (T_0 + T_1)/2$

$$\left.\frac{\partial T}{\partial z}\right|_{z=0} = \frac{T_1 - T_0}{\Delta z} \quad \text{and} \quad T^4\big|_{z=0} = \left(\frac{T_0 + T_1}{2}\right)^4 \quad \text{with} \quad \Delta z = 2z_1$$

$T = T_r + T'$ $\qquad T_r$ is a reference temperature around which we linearize

$$\begin{aligned}
Q + k_{1/2}\frac{T_1 - T_0}{\Delta z} &= \epsilon \sigma \left(\frac{2T_r + T_0' + T_1'}{2}\right)^4 \\
&\approx \epsilon \sigma T_r^4 + 2\epsilon \sigma T_r^3 (T_0' + T_1') \\
&= -3\epsilon \sigma T_r^4 + 2\epsilon \sigma T_r^3 (T_0 + T_1)
\end{aligned}$$

$T_0 \left(\frac{k_{1/2}}{\Delta z} + B(T_r)\right) = Q + 3\epsilon \sigma T_r^4 + T_1 \left(\frac{k_{1/2}}{\Delta z} - B(T_r)\right)$ where $B(T_r) = 2\epsilon \sigma T_r^3$

introduce $a = (Q + 3\epsilon \sigma T_r^4) / \left(\frac{k}{\Delta z} + B\right)$ and $b = \left(\frac{k_{1/2}}{\Delta z} - B\right) / \left(\frac{k_{1/2}}{\Delta z} + B\right)$

$$-\alpha_1 T_2^{n+1} + (1 + \alpha_1 + \gamma_1 - \gamma_1 b^n)T_1^{n+1} = \alpha_1 T_2^n + (1 - \alpha_1 - \gamma_1 + \gamma_1 b^n)T_1^n + \gamma_1 \frac{Q^n + Q^{n+1} + 6\epsilon \sigma T_r^4}{\frac{k_{1/2}}{\Delta z} + B^n}$$

define $\beta = \frac{\Delta t}{(\rho c)_1}\frac{1}{2\Delta z^2}$, then $\alpha_1 = \beta k_{3/2}$ and $\gamma_1 = \beta k_{1/2}$

$$\text{surface temperature} \quad T_s = \frac{1}{2}(T_1 + T_0) = \frac{1}{2}\left(\frac{Q + 3\epsilon \sigma T_r^4}{k_{1/2}/\Delta z + B} + T_1 + bT_1\right) = \frac{Q + 3\epsilon \sigma T_r^4 + \frac{2k}{\Delta z}T_1}{2(k_{1/2}/\Delta z + B)}$$

choose $T_r^n = T_s^n$
implemented in `conductionQ.f`. Note that the uppermost layer is a half-layer, and the first few grid points must be chosen as $z_0 = 0$ and $z_2 = 3z_1$ (in other words $z_1 = \Delta z/2$, $z_2 = z_1 + \Delta z$). The

coefficients for the nonlinear upper boundary condition are designed for that. Subroutine `setgrid` can be used to generate an appropriate grid.

Modified treatment of the upper boundary condition helpful in some situations: The linearization of the Stefan-Boltzmann law, σT^4, works well as long as the surface temperature changes slowly. The above approximation works very well for most situations, such as Mars orbit and a horizontal surface. A temporary instability, where the surface temperature overshoots significantly, was encountered in two situations: i) a sloped, shadowed surface emerges into sunlight. In this case the direct irradiance changes abruptly, and it is understandable that a discontinuity in the energy input leads to problems. ii) For asteroid orbits with high eccentricity and very small perihelion distances, when the pole emerges from winter into sunlight near perihelion. This transition is continuous, but the change in input energy is nevertheless dramatic.

Above, the thermal emission is linearized around the reference temperature $T_r^n = T_s^n$. If T_s^{n+1} is far from T_s^n, a significant error was incurred in the evaluation of the emitted energy. This can be addressed by repeating the calculation with a new reference temperature T_r somewhere in between T_s^n and T_s^{n+1}. And empirical choice is $T_r = \sqrt{T_s^n T_s^{n+1}}$. The geometric mean is a better choice than the arithmetic mean, because it tames large overshoots quicker. This method is essentially a predictor-corrector step, iteratively applied until T_r is within 20% of $T_s^{(n)}$. It seems this iterative method always converges.

Another approach is "artificial flux smoothing" where the time step is subdivided into many substeps, using linear interpolation of the incoming flux from Q^n to Q^{n+1}. However, this does not answer how a nascent instability is identified or how many substeps are required to cure it.

1.1.2 Upper boundary condition: prescribed T

standard formulas (1.2,1.3) with $T_0 = T_s$ and $z_0 = 0$

$$\alpha_1 = \frac{\Delta t}{(\rho c)_1} \frac{k_{3/2}}{(z_2 - z_1)z_2}, \qquad \gamma_1 = \frac{\Delta t}{(\rho c)_1} \frac{k_{1/2}}{z_1 z_2}$$

$$-\alpha_1 T_2^{n+1} + (1 + \alpha_1 + \gamma_1)T_1^{n+1} = \alpha_1 T_2^n + (1 - \alpha_1 - \gamma_1)T_1^n + \gamma_1(T_s^n + T_s^{n+1})$$

implemented in `conductionT.f`

1.1.3 Lower boundary condition

(assume $z_{N+1} - z_N = z_N - z_{N-1} =: \Delta z$)
No heat flux: $F_{N+\frac{1}{2}} = 0 \quad \Rightarrow \quad k_{N+\frac{1}{2}}(T_{N+1} - T_N) = 0 \quad \Rightarrow \quad T_{N+1} = T_N$

$$(1 + \gamma_N)T_N^{n+1} - \gamma_N T_{N-1}^{n+1} = (1 - \gamma_N)T_N^n + \gamma_N T_{N-1}^n$$

$$\gamma_N = \frac{\Delta t}{(\rho c)_N} \frac{k_{N-\frac{1}{2}}}{2(z_N - z_{N-1})^2}$$

Or geothermal heating: $F_{N+\frac{1}{2}} = F_{\text{geothermal}} \quad \Rightarrow \quad k_{N+\frac{1}{2}}(T_{N+1} - T_N) = \Delta z F_{\text{geothermal}}$

$$(1 + \gamma_N)T_N^{n+1} - \gamma_N T_{N-1}^{n+1} = (1 - \gamma_N)T_N^n + \gamma_N T_{N-1}^n + \frac{\Delta t}{(\rho c)_N} \frac{F_{\text{geothermal}}}{\Delta z}$$

1.2 Other Model Components

1.2.1 Seasonal frost cover (Mars)

Add latent heat of CO_2 sublimation

$$Q + k \left. \frac{\partial T}{\partial z} \right|_{z=0} = \left. \epsilon \sigma T^4 \right|_{z=0} + L \frac{dm_{CO_2}}{dt} \tag{1.5}$$

call `conductionQ` if T_s is above CO_2 frost point or if $m_{CO_2} = 0$; call `conductionT` if T_s is below CO_2 frost point or if $m_{CO_2} > 0$; calculate energy difference and add CO_2 mass; adjust surface albedo; repeat this at every time step

1.2.2 Influence of ice on thermal properties

This is only one possible parametrization. In retrospective, it agrees well with the laboratory measurements by Siegler et al. (2012) for vapor-deposited ice.

$$\begin{aligned} \rho c &= (1-\epsilon)\rho_{\text{regolith}} c_{\text{regolith}} + \epsilon f \rho_{\text{ice}} c_{\text{ice}} \\ k &= (1-\epsilon) k_{\text{regolith}} + \epsilon f k_{\text{ice}} + (1-f)\epsilon k_{\text{air}} \end{aligned}$$

ρ ... density; c ... heat capacity; k ... thermal conductivity
ϵ ... porosity (void space / total volume)
f ... ice filling fraction ($f = \rho_f / \rho_{\text{ice}}$, $\rho_f =$density of free ice)
Observed from orbit is ice-three thermal inertia I.

at around 200 Kelvin: $c_{\text{ice}} \approx 1540$ J/(kg K), $\rho_{\text{ice}} \approx 927$ kg/m³, $k_{\text{ice}} \approx 3.2$ W/(m K)
See Winter and Saari (1969) for heat capacity of silicates as a function of temperature.
See Handbook of Chemistry and Physics (Lide, 2003) for temperature dependence for ice.

In the program, k and ρc are defined on half-points, while ρ_f and T are defined on grid points.

1.2.3 Mars atmosphere

The elevation β of the sun above an horizontal horizon is given in terms of geographic latitude λ, declination δ of the sun, and the hour angle h:

$$\sin \beta = \cos \lambda \cos \delta \cos h + \sin \lambda \sin \delta. \tag{1.6}$$

The direct solar insolation is

$$Q_{\text{solar}} = \frac{S_0}{R^2}(1-A)(1-f)^{1/\max(\sin \beta, 0.04)} \sin \beta, \tag{1.7}$$

where S_0 is the solar constant, R the distance from the sun in AU, A the albedo, and f due to the extinction in the atmosphere. The length of the path through the atmosphere is proportional to $1/\sin \beta$ and the transmission is taken to be exponential in this path length. The nadir optical depth of the atmosphere is $-\ln(1-f) \approx f$. For small extinction and away from the horizon,

$(1 - f)^{1/\sin\beta} \approx 1 - f/\sin\beta$. The maximum atmospheric path length $\ell_{\max}$ is limited due to the curvature of the planet, $H/\ell_{\max} \approx \sqrt{H/2R} \approx 0.04$ for Mars, where H is the scale height of the atmosphere and R the radius of the planet.

Atmospheric emission is approximated by a fraction $f_{\rm IR}$ (typically 2–4%) of noontime insolation and is kept constant throughout a solar day (Kieffer et al., 1977):

$$Q_{\rm a,IR} = f_{\rm IR} \frac{S_0}{R^2} \sin\beta_{\rm noon} \qquad \text{(all day)} \tag{1.8}$$

This approximation fails in the polar regions; in this case, Kieffer et al. (1977) replaces the noontime insolation with the surface frost emission.

In addition, there is scattered light when $\sin\beta > 0$, which is approximated by

$$Q_{\rm a,scat} = \frac{1}{2} f_{\rm scat} \frac{S_0}{R^2}. \tag{1.9}$$

Half of the scattered light is assumed to be lost to space.

For the purpose of discussion, we determine the total energy budget of the atmosphere for a horizontal land mass. To first order $(1 - f)^{1/\sin\beta} \sin\beta \approx \sin\beta - f$, in eq. (1.7), so at any time the sun is above the horizon the energy absorbed and scattered in the atmosphere is approximately $(S_0/R^2)f$. Over a solar day

$$\frac{S_0}{R^2} f \int_{\rm daytime} dh \approx \frac{S_0}{R^2} \pi f. \tag{1.10}$$

The infrared emission from the atmosphere over the same time period is

$$2\pi f_{\rm IR} \frac{S_0}{R^2} \sin\beta_{\rm noon} \tag{1.11}$$

and the scattered energy

$$\pi f_{\rm scat} \frac{S_0}{R^2}. \tag{1.12}$$

The globally averaged $\sin\beta_{\rm noon}$ is

$$\frac{1}{\pi} \int_{-\pi/2}^{\pi/2} d\lambda \cos\lambda \sin\beta_{\rm noon} \approx \frac{1}{\pi} \int_{-\pi/2}^{\pi/2} d\lambda \cos^2\lambda = \frac{1}{2} \tag{1.13}$$

Global balance, (1.10)=(1.11)+(1.12), is achieved with

$$f = f_{\rm IR} + f_{\rm scat}.$$

This relation does not hold at an individual latitude, but it does hold globally.

This model was used in Schorghofer and Aharonson (2005) and in many subsequent modeling papers.

1.3 Semi-Implicit Scheme for Spherical Geometry

Governing equation (1.1) is appropriate for depths small compared to the radius of the body. In the context of small asteroids, it may be necessary to include the curvature effect. A 1-dimensional spherically-symmetric semi-implicit heat solver has been implemented (subroutine `conductionT_sphere` in `sphere1d_implicit.f90`) and will be described in a future publication ($\sim$2020). Conceptually, the derivation is the same as in section 1.1. The implementation is limited to uniform thermal properties and constant grid spacing.

Bibliography

H. H. Kieffer, T. Z. Martin, A. R. Peterfreund, B. M. Jakosky, E. D. Miner, and F. D. Palluconi. Thermal and albedo mapping of Mars during the Viking primary mission. *J. Geophys. Res.*, 82: 4249, 1977.

D. R. Lide, editor. *CRC Handbook of Chemistry and Physics*. CRC Press, 84th edition, 2003.

N. Schorghofer and O. Aharonson. Stability and exchange of subsurface ice on Mars. *J. Geophys. Res.*, 110(E5):E05003, 2005.

M. Siegler, O. Aharonson, E. Carey, M. Choukroun, T.L. Hudson, N. Schorghofer, and S. Xu. Measurements of thermal properties of icy Mars regolith analogs. *J. Geophys. Res.*, 117:E03001, 2012.

D. F. Winter and J. M. Saari. A particulate thermophysical model of the lunar soil. *Astrophys. J.*, 156:1135–1151, 1969.

Part 2

Diffusion of Water Vapor with Phase Transitions

1-Dimensional Diffusion of Water Vapor in Porous Medium with Phase Transitions;
variable diffusivity; irregular grid
3 phases: vapor, free (macroscopic) H_2O ice, H_2O adsorbate
implemented in `vapordiffusioni.f`

History: developed 2003–2004

2.1 Governing Equations

indices: v ... gas (vapor), f ... free ice (solid), a ... adsorbed water
$\bar{\rho}$ ... mass per total volume, $\bar{J}$ ... vapor flux per total area

conservation of mass:
$$\frac{\partial}{\partial t}(\bar{\rho}_v + \bar{\rho}_f + \bar{\rho}_a) + \nabla \cdot \bar{J} = 0 \tag{2.1}$$

vapor transport: (Landau and Lifshitz, 1987, Vol. VI, §57, §58)

$$J = -D\rho_0 \nabla c \tag{2.2}$$

c ... concentration $c = \rho_v/\rho_0$
ρ_{air} ... total density of air, including humidity
ρ_v ... density of vapor

$$p_v = nkT = \rho_v \frac{k}{m_v} T \tag{2.3}$$

m ... mass of molecule; k ... Boltzmann constant

adsorption: $\bar{\rho}_a = A(p, T)$
The amount adsorbed also changes when ice is present.

ϵ ... porosity (= void space / total volume)
$\epsilon(1 - \rho_f/\rho_{\text{ice}})$ ... fraction of space available to gas

$\bar{\rho}_v = \rho_v \epsilon (1 - \rho_f / \rho_{\text{ice}})$ $\qquad$ ρ_v ... vapor density in void space
$\bar{\rho}_f = \rho_f \epsilon$ $\qquad\qquad\qquad$ ρ_f ... ice density in volume not occupied by regolith
$\bar{J} = J \epsilon (1 - \rho_f / \rho_{\text{ice}})$ $\qquad$ J ... vapor flux through void area
$\rho_{\text{ice}} \approx 926 \text{ kg/m}^3$ ... density of ice when it's really cold

Conservation of mass becomes

$$\frac{\partial}{\partial t}\left(\rho_v\left(1 - \frac{\rho_f}{\rho_{\text{ice}}}\right) + \rho_f + \frac{1}{\epsilon}\bar{\rho}_a\right) + \partial_z\left(1 - \frac{\rho_f}{\rho_{\text{ice}}}\right)J = 0$$

$$\frac{\partial}{\partial t}\left[\rho_v\left(1 - \frac{\rho_f}{\rho_{\text{ice}}}\right) + \rho_f + \frac{1}{\epsilon}\bar{\rho}_a\right] = \partial_z\left[\left(1 - \frac{\rho_f}{\rho_{\text{ice}}}\right)D\partial_z\rho_v\right]$$

introduce $\varphi = 1 - \dfrac{\rho_f}{\rho_{\text{ice}}}$ and $\gamma = \dfrac{k}{m}\dfrac{1}{\epsilon}$

$$\partial_t\left(\frac{p}{T}\varphi + \frac{k}{m_v}\rho_f\right) + \gamma\left(\frac{\partial\bar{\rho}_a}{\partial p}\partial_t p + \frac{\partial\bar{\rho}_a}{\partial T}\partial_t T\right) = \partial_z\left[D\varphi\left(\partial_z\frac{p}{T}\right)\right] \qquad (2.4)$$

This is an equation for p and ρ_f.

If there is no ice, then

$$\left(\frac{1}{T} + \gamma\frac{\partial\bar{\rho}_a}{\partial p}\right)\partial_t p + \left(-\frac{p}{T^2} + \gamma\frac{\partial\bar{\rho}_a}{\partial T}\right)\partial_t T = \partial_z\left(D\partial_z\frac{p}{T}\right)$$

2.2   Discretizations

2.2.1   Possible discretizations of spatial derivatives

Note: These spatial discretizations are not necessarily optimal in terms of discretization error.

$$\partial_z(a\partial_z b)|_j = \frac{1}{\Delta z^2}\left(a_{j+1/2}(b_{j+1} - b_j) - a_{j-1/2}(b_j - b_{j-1})\right) + O(\Delta z^2) \qquad (2.5)$$

or

$$\partial_z(a\partial_z b)|_j = \frac{1}{2\Delta z^2}\left((a_{j+1} + a_j)(b_{j+1} - b_j) - (a_j + a_{j-1})(b_j - b_{j-1})\right) + O(\Delta z^2) \qquad (2.6)$$

or

$$\begin{aligned}
\partial_z(a\partial_z b)|_j &= a\partial_{zz}b + (\partial_z a)\partial_z b \\
&= \frac{1}{\Delta z^2}\left(a_j(b_{j+1} - 2b_j + b_{j-1}) + \frac{1}{4}(a_{j+1} - a_{j-1})(b_{j+1} - b_{j-1})\right) + O(\Delta z^2) \quad (2.7)
\end{aligned}$$

The most general discretization which is accurate to $O(\Delta z^2)$, rather than just $O(\Delta z)$, is of the following form (mathematica notebook discretization2.nb)

$$
\begin{aligned}
\partial_z(a\partial_z b)|_j \;=\;& \frac{1}{\Delta z^2}\Big(ca_j b_j + (-1-\tfrac{c}{2})a_{j-1}b_j + (-1-\tfrac{c}{2})a_{j+1}b_j \\
& -\frac{c}{2}a_j b_{j-1} + \frac{3+c}{4}a_{j-1}b_{j-1} + \frac{1+c}{4}a_{j+1}b_{j-1} \\
& -\frac{c}{2}a_j b_{j+1} + \frac{1+c}{4}a_{j-1}b_{j+1} + \frac{3+c}{4}a_{j+1}b_{j+1}\Big) + O(\Delta z^2)
\end{aligned}
\tag{2.8}
$$

Choices (2.6) and (2.7) above correspond to $c = -1$ and $c = -2$, respectively.

Another set of schemes does not involve the cross-terms $a_{j+1}b_{j-1}$ and $a_{j-1}b_{j+1}$. They are of the following form (mathematica notebook discretization3.nb)

$$
\begin{aligned}
\partial_z(a\partial_z b)|_j \;=\;& \frac{1}{\Delta z^2}\big(-a_j b_j - ca_{j-1}b_j + (-1+c)a_{j+1}b_j + \\
& (1-c)a_j b_{j-1} + ca_{j-1}b_{j-1} + ca_j b_{j+1} + (1-c)a_{j+1}b_{j+1}\big) + \\
& \left(c - \frac{1}{2}\right)O(\Delta z) + O(\Delta z^2)
\end{aligned}
\tag{2.9}
$$

$$
= \frac{1}{\Delta z^2}\left[(1-c)a_{j+1}(b_{j+1}-b_j) + ca_{j-1}(b_{j-1}-b_j) + a_j(cb_{j+1}-b_j+(1-c)b_{j-1})\right] + O(\Delta z)
$$

For $c = 1/2$ this reduces to scheme (2.6) above
If starting with complete pore filling, $c > 0$ is required for downward motion of ice table.

On irregular grid: General scheme without cross-terms (mathematica notebook discretization6.nb)

$$
\begin{aligned}
\partial_z(a\partial_z b)|_j \;=\;& -\frac{2c + (1-2c)h_+/h_-}{h_- h_+}a_j b_j + \frac{-1 + (1-2c)h_+/h_-}{h_-(h_- + h_+)}a_{j-1}b_j + \frac{2c-2}{h_+(h_- + h_+)}a_{j+1}b_j + \\
& +\frac{1 + (1-2c)h_+/h_-}{h_-(h_- + h_+)}a_j b_{j-1} + \frac{1 + (2c-1)h_+/h_-}{h_-(h_- + h_+)}a_{j-1}b_{j-1} + \frac{2c}{h_+(h_- + h_+)}a_j b_{j+1} \\
& +\frac{2-2c}{h_+(h_- + h_+)}a_{j+1}b_{j+1} + O(h_+ + h_-)
\end{aligned}
\tag{2.10}
$$

where $h_+ = z_{j+1} - z_j$ and $h_- = z_j - z_{j-1}$. For $h_+ = h_- = h$ this reduces to (2.9)

2.2.2 Discretization of time derivative

use eq. (2.4), $A \equiv f$

$$
\begin{aligned}
& \frac{p_j^{n+1}}{T_j^{n+1}}\varphi_j^{n+1} - \frac{p_j^n}{T_j^n}\varphi_j^n + \frac{k}{\mu}\left(\rho_{f\,j}^{n+1} - \rho_{f\,j}^n\right) + \gamma\left.\frac{\partial f}{\partial p}\right|_j^n (p_j^{n+1} - p_j^n) + \\
& \qquad\qquad +\gamma\left.\frac{\partial f}{\partial T}\right|_j^n (T_j^{n+1} - T_j^n) = \Delta t\left(\partial_z D\varphi \partial_z \frac{p}{T}\right)_j^n
\end{aligned}
\tag{2.11}
$$

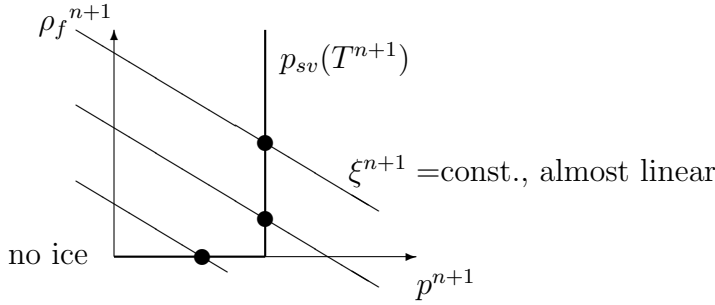derivatives of the isotherm are not expanded to keep it linear

12

2.2.3 Complete scheme

using (2.11) and (2.10)

$$
\begin{aligned}
\xi_j^{n+1} \;=\;& \frac{p_j^n}{T_j^n}\varphi_j^n + \frac{k}{\mu}\rho_{fj}^{\,n} + \gamma\left.\frac{\partial f}{\partial p}\right|_j^n p_j^n - \gamma\left.\frac{\partial f}{\partial T}\right|_j^n (T_j^{n+1}-T_j^n) + \\
& \frac{\Delta t}{\Delta z^2}\left[D_j\varphi_j^n\left(\frac{p_{j+1}^n}{T_{j+1}^n} - 2\frac{p_j^n}{T_j^n} + \frac{p_{j-1}^n}{T_{j-1}^n}\right) + \frac{1}{4}(D_{j+1}\varphi_{j+1}^n - D_{j-1}\varphi_{j-1}^n)\left(\frac{p_{j+1}^n}{T_{j+1}^n} - \frac{p_{j-1}^n}{T_{j-1}^n}\right)\right]
\end{aligned}
$$

where $\xi^{n+1} = \dfrac{p^{n+1}}{T^{n+1}}\left(1 - \dfrac{\rho_f^{n+1}}{\rho_{\text{ice}}}\right) + \dfrac{k}{\mu}\rho_f^{\,n+1} + \gamma\left.\dfrac{\partial f}{\partial p}\right|^n p^{n+1}$

$p \le p_{sv}(T)$ and $0 \le \rho_f \le \rho_{\text{ice}}$

$\rho_f{}^{n+1}$

$p_{sv}(T^{n+1})$

ξ^{n+1} =const., almost linear

no ice

p^{n+1}

p_{sv} ... saturation vapor pressure

Try $\rho_f^{n+1} = 0 \quad\Rightarrow\quad p^{n+1} = \dfrac{T^{n+1}\cdot\xi^{n+1}}{1 + T^{n+1}\gamma\left.\frac{\partial f}{\partial p}\right|^n}$ and $\rho_f^{n+1} = 0$

If $\quad p^{n+1} > p_{sv}(T^{n+1}) \quad$ then $\quad p^{n+1} = p_{sv}(T^{n+1}) \qquad$ and

$$
\rho_f^{n+1} = \frac{\xi^{n+1} - \frac{p_{sv}(T^{n+1})}{T^{n+1}} - \gamma\left.\frac{\partial f}{\partial p}\right|^n p_{sv}(T^{n+1})}{\frac{k}{\mu} - \frac{p_{sv}(T^{n+1})}{T^{n+1}\rho_{\text{ice}}}}
$$

introduce $\quad p_{\text{frost}}^{n+1} = p_{sv}(T^{n+1})$

2.2.4 Upper boundary condition

1) $p(z=0,t) = p_{\text{atm.}}(t)$
2) $D(z=0) = D_0$
3) $\varphi_0 = 1$

$$
\left.\partial_z\left(D\varphi\partial_z\frac{p}{T}\right)\right|_{j=0} = \frac{1}{\Delta z^2}\left[D_1\varphi_1\left(\frac{p_2}{T_2} - 2\frac{p_1}{T_1} + \frac{p_{\text{atm}}}{T_{\text{surf}}}\right) + \frac{1}{4}(D_2\varphi_2 - D_0\varphi_0)\left(\frac{p_2}{T_2} - \frac{p_{\text{atm}}}{T_{\text{surf}}}\right)\right] \quad (2.12)
$$

13

for half-shifted grid ($z_2 = 3z_1$):

$$a\partial_{zz}b + (\partial_z a)\partial_z b = \frac{1}{\Delta z^2}\left[a_1\left(\frac{8}{3}b_s - 4b_1 + \frac{4}{3}b_2\right) + \left(-\frac{4}{3}a_s + a_1 + \frac{1}{3}a_2\right)\left(-\frac{4}{3}b_s + b_1 + \frac{1}{3}b_2\right)\right]$$
$$(2.13)$$

2.2.5 Lower boundary condition

no vapor flux (impermeable) $J = 0 \quad \Rightarrow \quad \partial_z \rho_v = 0 \quad \Rightarrow \quad \partial_z \frac{p}{T} = 0 \quad \Rightarrow \quad \frac{p_{N+1}}{T_{N+1}} = \frac{p_{N-1}}{T_{N-1}}$

$$\partial_z\left(D\varphi\partial_z\frac{p}{T}\right)\Big|_{j=N} = \frac{1}{\Delta z^2}2D_N\varphi_N\left(\frac{p_{N-1}}{T_{N-1}} - \frac{p_N}{T_N}\right) \tag{2.14}$$

2.3 Numerical Stability

von Neumann stability analysis has been carried out for various variants of the scheme; this is only relevant for discussion purposes. Typeset notes are available upon request.

Used in Schorghofer and Aharonson (2005)

Bibliography

L. D. Landau and E. M. Lifshitz. *Fluid Mechanics*. Pergamon Press, Oxford, 1987.

N. Schorghofer and O. Aharonson. Stability and exchange of subsurface ice on Mars. *J. Geophys. Res.*, 110(E5):E05003, 2005.

Part 3

Long-Term Ice Evolution

Long-term evolution of sub-surface ice due to loss to space (for asteroids) or exchange with the atmosphere (for Mars) using diurnally-resolved temperatures

History:
    2002–2004 equilibrium ice table on Mars
    2006–2011 asynchronous model for ice on Mars (where re-charge can occur)
    2013–2017 asynchronous model for asteroids (where impact-gardening occurs)

3.1   Equilibrium Models of Near-Surface Ice on Mars

The equilibrium depth to the ice table is defined by a balance between the vapor pressure at the ice table and the atmosphere. It is the end result of atmosphere-subsurface vapor exchange after an asymptotically long time. If no equilibrium is possible, then subsurface ice is "unstable". Using the thermal model described in Part 1, this model calculates the equilibrium depth based on matching the vapor density at the ice table with that in the atmosphere. The thermal model is run over a number of years (orbits) to equilibrate, and annual means are taken from the last orbit. As the ice content of the subsurface changes the thermal properties, the thermal model is repeatedly equilibrated. The code deploys an iterative root-finding procedure, using the bisection method. The iterations are performed by `mars_mapi.f`, which finds the equilibrium depth. Then `mars_mapt2.f` can be used to output additional variables for a given ice table depth.

   The model is extensively used in Schorghofer and Aharonson (2005), where further description is available. With extensions described in section 5.2 for planar slopes, it also forms the core of the model used in Aharonson and Schorghofer (2006).

3.2   Asynchronous Model for Ice on Mars

Schorghofer (2010) provides a description of this rather complex model, which is not repeated here. In brief, the model couples a diurnally-resolved thermal model with a long-term ice evolution model. Ice (massive or interstitial) can be lost to the atmosphere and, vice-versa, pore spaces can be recharged with interstitial ice. Details of the long-term ice evolution model are also described in this paper, which involve a one-sided derivative at the moving ice table; otherwise a numerical instability occurs due to the strong contrast in thermal properties at the ice table. The model

allows for up to three layers: dry, soil with interstitial ice (plus air), and massive ice with dust. In the current implementation, one of the two interfaces is tracked explicitly. The model is extensively used in Schorghofer (2007) and Schorghofer and Forget (2012) for studies of the Martian Ice Age cycle.

3.3 Asynchronous Model for Temperature, Impact Stirring, and Ice Loss on Asteroids

Schorghofer (2016) describes this model and applies it to (1) Ceres and (7968) Elst-Pizarro. In brief, it combines diurnally-resolved temperatures, probabilistic impact stirring (only one-dimensional), and the long-term loss of near-surface ice to space. It was also used for the ice retreat calculations published in Prettyman et al. (2017). The main program is `asteroid_fast2`.

A significant complexity in this model arises from partially ice-filled pore spaces (necessary to incorporate the consequences of impact stirring), because the re-distribution of ice within the pores due to vapor diffusion and deposition adds another governing equation. This redistribution turned out to be negligible in all cases it was considered. A simpler two-layer version, where pore spaces are either empty or full, is implemented in `asteroid_fast1`, which is similar to the model described in the supporting information of Sizemore et al. (2017).

Bibliography

O. Aharonson and N. Schorghofer. Subsurface ice on Mars with rough topography. *J. Geophys. Res.*, 111(E11):E11007, 2006.

T. H. Prettyman et al. Extensive water ice within Ceres' aqueously altered regolith: Evidence from nuclear spectroscopy. *Science*, 355:55–59, 2017.

N. Schorghofer. Dynamics of ice ages on Mars. *Nature*, 449(7159):192–194, 2007.

N. Schorghofer. Fast numerical method for growth and retreat of subsurface ice on Mars. *Icarus*, 208(2):598–607, 2010.

N. Schorghofer. Predictions of depth-to-ice on asteroids based on an asynchronous model of temperature, impact stirring, and ice loss. *Icarus*, 276:88–95, 2016.

N. Schorghofer and O. Aharonson. Stability and exchange of subsurface ice on Mars. *J. Geophys. Res.*, 110(E5):E05003, 2005.

N. Schorghofer and F. Forget. History and anatomy of subsurface ice on Mars. *Icarus*, 220(2): 1112–1120, 2012.

H. G. Sizemore et al. Pitted terrain on dwarf planet Ceres and implications for volatiles. *Geophys. Res. Lett.*, 44:6570–6578, 2017.

Part 4

Terrestrial Analogs

1-Dimensional Thermal Model, 0-Dimensional Terrestrial Atmosphere, 3-Dimensional Insolation Model (terrain shadowing)

History:
   2013–2016 Mauna Kea, Hawaii (sec. 4.1 and 5)
   2004–2005 Beacon Valley, Antarctica (sec. 4.2)

Sun position as a function of date is based on Blanco-Muriel et al. (2001), translated into Fortran. It provides the zenith angle and azimuth of the sun, and the Earth-sun distance. Implemented in `sunpos.f90`

4.1   Mauna Kea atmosphere

calculate clear-sky direct and indirect short-wave irradiance on Mauna Kea in W/m^2
mostly based on Nunez (1980), corrected for typos. Implemented in `mk_atmosphere.f90`

Z ... solar zenith angle (radians)
I_0 ... clear-sky direct irradiance; D_0 ... clear-sky diffuse irradiance
R ... Earth-sun distance in AU
m, m' ... optical air mass (unitless)
p_0 ... total pressure (Pa)
w ... precipitable water vapor (cm)
Transmission coefficients:
ψ_{wa} ... water vapor absorption; ψ_{ws} ... water vapor scattering
ψ_{rs} ... Rayleigh scattering
ψ_{da} ... dust absorption; ψ_{ds} ... dust scattering

Relative air mass:
simplest approximation: $m = 1/\cos Z$
better approximation (Kasten, 1966):

$$m = \frac{1}{\cos Z + 0.15 \times (93.885 - Z)^{-1.253}} \tag{4.1}$$

17

if $(m < 0)$, then $m = \infty$
$p_0 = 610$ on Mauna Kea summit
$m' = m \times p_0/1013$

Water vapor:
$w = 0.16$ cm for Mauna Kea, according to www.gemini.edu/sciops/telescopes-and-sites/observing-condition-constraints/mk-water-vapour-statistics

$$\psi_{wa} = 1 - 0.077(wm)^{0.30} \quad \text{McDonald (1960)} \tag{4.2}$$
$$\psi_{ws} = 1 - 0.025wm \tag{4.3}$$

Rayleigh scattering: 8% at sea level according to Fig 3-3 in Bird and Hulstrom (1981)

$$\psi_{rs} = \exp(-0.08m') \tag{4.4}$$

Aerosols: aerosol optical depth on Mauna Kea $= 0.0084 \times (\lambda/1\mu m)^{-1.26}$ (Buton et al., 2013)

$$\psi_{ds} = \exp(-m \times 0.0084 \times 0.5^{-1.26}) \tag{4.5}$$
$$\psi_{da} = \psi_{ds} \quad \text{assumes single scattering albedo of 0.5} \tag{4.6}$$

Direct sunlight:
$$I_0 = \psi_{wa}\psi_{da}\psi_{ws}\psi_{rs}\psi_{ds} \times (\text{solar constant})/R^2 \tag{4.7}$$
(without the last factor, this is the transmittance)

Diffuse sunlight:
$$D_0 = I_0 \cos(Z)\psi_{wa}\psi_{da}\frac{1 - \psi_{ws}\psi_{rs}\psi_{ds}}{2} \tag{4.8}$$
Roundoff issue: if $(D_0 \leq 0)$, then $D_0 = 0$ because of -0.

Total short-wavelength flux:
$$F = I_0 \cos Z + D_0 \tag{4.9}$$
Roundoff issue: if $(F \leq 0)$, then $F = 0$ because of -0.

Not included are the sensible heat flux and long-wave downward radiation.

Atmospheric contribution with terrain shadowing: see Part 5 and references therein.

used in Schorghofer et al. (2017) and Schorghofer (2018)

4.2   Dry Valleys of Antarctica

This model calculates the loss of buried ice to the atmosphere, and involves molecular diffusion in an air-H_2O mixture, including the advective contribution. The equations underlying this model are described in Schorghofer (2005). The source code has not been readied for distribution and no further documentation was written. By now this model has been superseded by implementations from other research groups.

Bibliography

R. E. Bird and R. L. Hulstrom. A simplified clear sky model for direct and diffuse insolation on horizontal surfaces. Technical report, Golden, Colorado, 1981. Report No. SERI/TR-642-761.

M. Blanco-Muriel, D. C. Alarcón-Padilla, T. López-Moratalla, and M. Lara-Coira. Computing the solar vector. *Solar Energy*, 70:431–441, 2001.

C. Buton et al. Atmospheric extinction properties above Mauna Kea from the Nearby SuperNova Factory spectro-photometric data set. *Astr. & Astrophys.*, 549:A8, 2013.

F. Kasten. Albedo and sky radiance measurements in Greenland. *Arch. Meteor. Geophys. Biokli-matol.*, B14:206–223, 1966.

J. E. McDonald. Direct absorption of solar radiation by atmospheric water vapor. *Journal of Meteorology*, 17:319–328, 1960.

M. Nunez. The calculation of solar and net radiation in mountainous terrain. *Journal of Biogeog-raphy*, 7:173–186, 1980.

N. Schorghofer. A physical mechanism for long-term survival of ground ice in Beacon Valley, Antarctica. *Geophys. Res. Lett.*, 32:L19503, 2005.

N. Schorghofer. Permafrost survey on the Maunakea summit plateau: Final report. Technical report, University of Hawaii, 2018. 28pp.

N. Schorghofer, M. Leopold, and K. Yoshikawa. State of high-altitude permafrost on tropical Maunakea volcano, Hawaii. *Permafrost and Periglacial Processes*, 28:685–697, 2017.

Part 5

3D Surface Energy Balance

Energy Balance with Horizons and Diffuse Irradiance from Land within Field of View

History:
    2002–2005 Planar slopes (sec. 5.2)
    2010–2019 3D topography (sec. 5.3–5.6)

With 3-dimensional topography the surface energy balance is modified, compared to a horizontal planar surface, for the following reasons:

   1) changed incidence angle,

   2) elevated horizons (terrain shadowing),

   3) reflected sunlight from visible land surfaces, and

   4) infrared emissions from visible land surfaces ("self-heating").

The incidence angle on a sloped surface is easily calculated. The elevated horizons change the time of sunset and sunrise, and also reduce the scattered radiation received from the atmosphere. Horizon determinations require that all other pixels in the domain are considered, so this is a non-local computational problem. Diffusively reflected sunlight and infrared emissions (indirect short-wavelength and long-wavelength irradiance) involve the same type of computational problem. They require the evaluation of "view factors", or an equivalent quantity, which describe the size of each surface element as seen from the point of interest. This is computationally even more demanding than the horizons calculations, in terms of number of required arithmetic operations, memory, and data transfer from memory.

5.1   Incidence Angle on Slope

The elevation β of the sun above a horizontal horizon is given in terms of geographic latitude λ, declination δ of the sun, and the hour angle h by

$$\sin \beta = \cos \lambda \cos \delta \cos h + \sin \lambda \sin \delta. \tag{5.1}$$

The angle θ of the sun above a sloped surface is

$$\sin \theta = \cos \alpha \sin \beta - \sin \alpha \cos \beta \cos(\Delta a), \tag{5.2}$$

20

where Δa is the difference between the azimuth of the sun and the azimuth of the topographic gradient. The sun is assumed to be below the horizon if either $\sin \beta < 0$ (horizontal horizon at infinity) or $\sin \theta < 0$ (self shadowing of slope). For 3D topography, a distant horizon, higher than the self shadowing slope, introduces an additional cutoff $e_{\max}$ (maximum horizon elevation).

On an airless body the direct insolation is

$$Q_{\text{solar}} = \frac{S_0}{R^2}(1 - A)\sin \theta. \tag{5.3}$$

where S_0 is the solar constant, R the distance from the sun in AU, and A the albedo.

5.2 Thermal Model for Tilted Planar Slope

Planar slopes are much simpler than the general 3D problem. This section describes a model for the thermal balance on a tilted plane, in the form of two coupled 1D thermal models, plus a 0D atmosphere. The model is for Mars, but easily simplified to airless bodies. It was used in Aharonson and Schorghofer (2006) and Schorghofer and Edgett (2006).

α ... slope angle

The heat balance on the surface is

$$Q(\alpha) + k \left.\frac{\partial T}{\partial z}\right|_{z=0} = \epsilon \sigma T^4 + (\text{latent heat of } CO_2 \text{ frost}) \tag{5.4}$$

with

$$Q = Q_{\text{solar}}(\alpha) + Q_{\text{a,IR}}(\alpha) + Q_{\text{a,scat}}(\alpha) + Q_{\text{land}}(\alpha). \tag{5.5}$$

Q is the incoming radiation from the sun, atmosphere, and surfaces within field of view, T temperature, z the vertical coordinate, k the thermal conductivity, ϵ emissivity, and σ the Stefan-Boltzmann constant. The subscript a denotes contributions from the atmosphere.

The direct solar insolation is

$$Q_{\text{solar}} = \frac{S_0}{R^2}(1 - A)(1 - f)^{1/\max(\sin \beta, 0.04)}\sin \theta, \tag{5.6}$$

where f due to the extinction in the atmosphere. This is a generalization of (1.7). The length of the path through the atmosphere is proportional to $1/\sin \beta$. The maximum atmospheric path length is limited due to the curvature of the planet, which motivates the threshold of 0.04, as described in subsection 1.2.3.

The calculation of the atmospheric absorption and scattering is modified from subsection 1.2.3 to involve a slope factor of $\cos^2(\alpha/2)$. This slope factor for the IR emission takes into account that a tilted surface facing a horizontal horizon sees only a restricted portion of the sky. It is unclear whether this is the best approximation, see Rakovec and Zakšek (2012). An isotropic flux is another commonly-used approximation for the shortwave diffusive flux (Flo Heggem et al., 2001).
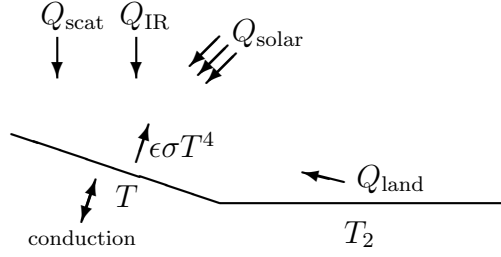
21

Figure 5.1: Contributions to the heat balance on a slope with surface temperature T.

Atmospheric emission is approximated by a fraction f_{IR} (typically 2–4%) of noontime insolation and is kept constant throughout a solar day (Kieffer et al., 1977):

$$Q_{\text{a,IR}} = f_{\text{IR}} \frac{S_0}{R^2} \cos^2\left(\frac{\alpha}{2}\right) \sin \beta_{\text{noon}} \qquad \text{(all day)} \tag{5.7}$$

$$Q_{\text{a,scat}} = \frac{1}{2} f_{\text{scat}} \frac{S_0}{R^2} \cos^2\left(\frac{\alpha}{2}\right) \qquad \text{when } \sin \beta > 0 \tag{5.8}$$

Spiga and Forget (2008) have derived a more detailed parameterization for $Q_{\text{a,scat}}$ on a planar slope.

The surface reemits radiation in all directions, but receives additional heat from surfaces in its field of view. This emission is weighted according to the incidence angles i and integrated over the spherical angle Ω subtended by the visible land surfaces. If we imagine a horizontal surface at uniform temperature T_2 (Kreslavsky and Head, 2005):

$$Q_{\text{land}} = \epsilon_2 \sigma T_2^4 \int \cos i \, d\Omega = \sin^2\left(\frac{\alpha}{2}\right) \epsilon_2 \sigma T_2^4. \tag{5.9}$$

If one assumes $T_2 = T$ and $\epsilon_2 = \epsilon$, then this term can be brought to the right-hand side of eq. (5.4), leading to an effective emissivity of $\epsilon \cos^2(\alpha/2)$. However, this is often not a good approximation. It is more accurate to base T_2 on a separate 1D model for a flat surface.

The equation of heat conduction is solved in the subsurface with a semi-implicit Crank-Nicolson scheme on a grid with spatially varying spacings, as described in Part 1 of the User Guide.

5.3   Horizons and View Factors

Shadowing by nearby topography (terrain shading) defines local horizons and is important for the energy balance. Horizons for each surface element are determined with azimuth rays, typically every 2° in azimuth, and the highest horizon in each direction is stored. For the purpose of horizon determination, the topography is represented by triangular surface elements. The horizon-finding calculation is implemented in `shadows.f90` and `shadow_subs.f90`.

The topography is defined on a rectangular coordinate grid with spatial resolution Δx in the longitude direction and Δy in the latitude direction. Curvature effects are not incorporated, i.e. the domain needs to be small compared to the radius of the body. Nor can the domain include the rotational pole. Surface normals are calculated using center-differences in x- and y-direction, and one-sided differences at the domain boundaries.

Use of spatial grids with various resolutions (multigrid method) dramatically accelerate the horizons calculation, because cells that are far from the point of interest are larger and fewer. For a domain with $N \times N$ pixels, the computational cost without multigrid method is $O(N^4)$. With multigrid, it is $O(N \log N)^2$. In the current implementation of the multigrid method, up to ten grids can be used, the coarsest has 2^{10-1} less resolution than the finest. If the multigrid method is not used, an optional cut-off radius `RMAX` can be introduced, so spatial distances larger than `RMAX` are ignored.

If only shadows (and direct insolation) are to be calculated, these horizon heights are all the geometric information that is needed. The view factor is calculated in terms of the spherical angle as viewed from the other element, $d\Omega$, and stored. Mutual visibility is determined by calculating the slope of the line that connects the two elements and comparing it to the maximum topographic slope along a ray in the same direction, tracing outward. (Hence there is a sort involved that is not necessary if only horizons are needed.) For the purpose of view factors, the topography is represented by rectangles. The view factor calculation is implemented in `fieldofviews.f90` and `fieldofview_subs.f90`. Neighbors in 8 directions are considered.

The results of these geometric calculations serve as input for insolation or thermal calculations.

5.4   Governing Equations for Scattering

The equation governing the energy balance on the surface is

$$(1 - A)(Q_{\text{direct}} + Q_{\text{refl}}) + k\frac{\partial T}{\partial z} + \epsilon Q_{\text{IR}} = \epsilon \sigma T^4 \tag{5.10}$$

where A is albedo, Q_{direct} incoming solar radiation (insolation), k thermal conductivity, T temperature, z depth below surfce, ϵ emissivity, and σ the Stefan-Boltzmann constant. The flux Q_{direct} is determined from the declination of the Sun, latitude, and hour angle, eqs. (5.1, 5.2). Due to topography, reflected sunlight (Q_{refl}) and thermal emission (Q_{IR}) from other surfaces need to be added.

The amount of sunlight diffusely reflected depends on the spherical angle $d\Omega$ subtended by the surface element, and similarly for infrared emission:

$$Q_{\text{refl}}(x, y) = \frac{1}{\pi} \iint A' \left[Q'_{\text{direct}} + Q'_{\text{refl}}\right] \cos\theta \, d\Omega(x, y, x', y') \tag{5.11}$$

$$Q_{\text{IR}}(x, y) = \frac{1}{\pi} \iint \left[\epsilon \sigma T'^4 + (1 - \epsilon)Q'_{\text{IR}}\right] \cos\theta \, d\Omega(x, y, x', y') \tag{5.12}$$

where primed variables are evaluated at (x', y') and unprimed variables at (x, y). The integrals are over all surface elements within the field of view, and θ is the local incidence angle of the straight line of sight that connects the two surface elements. Equations (5.11) and (5.12) turn into an explicit time-stepping procedure when Q'_{refl} and Q'_{IR} on the right hand side are evaluated at the previous time step. The term with the factor $(1 - \epsilon)$ is reflected infrared.

In the literature these equations are often written in terms of a "view factor"

$$V_{ij} = \frac{\cos\theta_i \cos\theta_j}{\pi r_{ij}^2} d\mathcal{A}_j$$

23

where r_{ij} is the distance between the two facets, $\theta_i = \theta(x, y)$, $\theta_j = \theta(x', y')$, and $\mathcal{A}$ the differential surface area. Since

$$d\Omega = \frac{\cos \theta_j}{r_{ij}^2} d\mathcal{A}_j$$

this is equivalent. The discretized equations then take on the form

$$Q_{\text{refl } i,j} = \sum_{i',j'} A_{i',j'} \left[Q_{\text{direct } i',j'} + Q_{\text{refl } i',j'} \right] V_{i,j,i',j'} \tag{5.13}$$

$$Q_{\text{IR } i,j} = \sum_{i',j'} \left[\epsilon \sigma T_{i',j'}^4 + (1 - \epsilon) Q_{\text{IR},i',j'} \right] V_{i,j,i',j'} \tag{5.14}$$

The model also includes 1D subsurface heat conduction, eq. (1.1). Subsurface temperatures need to be equilibrated, and hence the entire model needs to be run much longer than would be necessary without subsurface heat. Lateral subsurface heat conduction is neglected. Without subsurface conduction, equilibrium temperatures, according to eq. (5.10) with $k = 0$, can be used, and only a few steps of equilibration are needed in this case.

The differential solid angle can be written as

$$d\Omega = \cos e \, de \, d\varphi \tag{5.15}$$

where φ is azimuth and e the elevation (an angle) above the horizon. The solid angle of the entire landscape within field of view is

$$\Omega_{\text{land}} = \iint d\Omega = \int_0^{2\pi} \int_0^{e(\varphi)} de \, d\varphi \cos e = \int_0^{2\pi} d\varphi \, \sin(e(\varphi)) \tag{5.16}$$

The size of the visible sky is $2\pi - \Omega_{\text{land}}$. The sky view factor F is the spherical angle of the visible sky divided by 2π. Hence, $F = 1 - \Omega_{\text{land}}/(2\pi)$. It is also helpful to introduce the abbreviation

$$G = \frac{1}{\pi} \iint \cos \theta \, d\Omega \tag{5.17}$$

For a half-sphere $G = 1$.

Next several special cases, with increasing complexity, are considered:

a) In the special case of a surface covered by a dome at uniform temperature,

$$\iint \cos \theta \, d\Omega = \int_0^{2\pi} d\varphi \int_0^{\pi/2} de \sin e \cos e = 2\pi \int_0^{\pi/2} de \sin e \cos e = 2\pi \frac{1}{2} \sin^2(\pi/2) = \pi$$

Hence $G = 1$ and (5.12) becomes $Q_{\text{IR}} = \epsilon \sigma T'^4$.

b) Planar slope with a single temperature combined with a horizontal surface with another temperature, as in Figure 5.1. In this case, $\Omega = 2\alpha$, so that at $\alpha = \pi/2$ a quarter of the sphere remains. For the slope, the horizon height $e(\varphi)$ along direction φ is related by $\tan \alpha \cos \varphi = \tan e$.

24

For integration practice,

$$\iint d\Omega = \int_{-\pi/2}^{\pi/2} d\varphi \int_0^{e(\varphi)} de \cos e = \int_{-\pi/2}^{\pi/2} d\varphi \sin(e(\varphi)) = \int_{-\pi/2}^{\pi/2} d\varphi \frac{\tan\alpha \cos\varphi}{\sqrt{1+\tan^2\alpha \cos^2\varphi}} = 2\alpha$$

where $\sin e = \tan e/\sqrt{1+\tan^2 e}$ was used. The integral of interest

$$
\begin{aligned}
\iint \cos\theta \, d\Omega &= \int_{-\pi/2}^{\pi/2} d\varphi \int_0^{e(\varphi)} de \sin e \cos e \\
&= \int_{-\pi/2}^{\pi/2} d\varphi \frac{1}{2} \sin^2(e(\varphi)) = \frac{1}{2}\int_{-\pi/2}^{\pi/2} d\varphi \frac{\tan^2\alpha \cos^2\varphi}{1+\tan^2\alpha \cos^2\varphi} \\
&= \frac{\pi}{2}(1-\cos\alpha) = \pi\sin^2\left(\frac{\alpha}{2}\right)
\end{aligned}
$$

In this case, $G = \sin^2(\alpha/2)$ and (5.12) becomes

$$Q_{\text{IR}} = \epsilon\sigma T'^4 \sin^2\left(\frac{\alpha}{2}\right)$$

plus the reflected infrared, which reproduces (5.9).

c) Uniform temperature, locally flat:

$$\iint \cos\theta \, d\Omega = \int_0^{2\pi} \int_0^{e(\varphi)} de \, d\varphi \cos e \sin e = \frac{1}{2}\int_0^{2\pi} d\varphi \sin^2(e(\varphi))$$

G is $\sin^2 e(\varphi)$ averaged over azimuths. For small e, $G \ll \Omega_{\text{land}}$.

d) Uniform temperature, not locally flat:

$$\sin\theta = \cos\alpha \sin\beta + \sin\alpha \cos\beta \cos(\Delta a)$$

where α is the local slope angle. There is now also a lower limit on the elevation angle, $e_{\min}(\varphi)$, from the self-shadowing of the slope, so $\sin\theta$ will never become negative, and therefore

$$\tan e_{\min} = -\tan\alpha \cos(\Delta a)$$

which can be positive or negative.

The integral of interest is

$$\iint \cos\theta \, d\Omega = \int_0^{2\pi} \int_{e_{\min}(\varphi)}^{e(\varphi)} de \, d\varphi \cos e \left[\cos\alpha \sin e + \sin\alpha \cos e \cos(\Delta a)\right] \qquad (5.18)$$

and the integrals over e can be computed as

$$
\begin{aligned}
\frac{1}{\pi}\int de \cos e \sin e &= \frac{1}{2\pi}\sin^2 e \\
\frac{1}{\pi}\int de \cos^2 e &= \frac{1}{2\pi}(e + \sin e \cos e)
\end{aligned}
$$

25

G can be pre-computed from static geometric information:

$$G = \frac{\cos\alpha}{2\pi} \int_0^{2\pi} d\varphi \left(\sin^2 e - \sin^2 e_{\min}\right) +$$

$$+ \frac{\sin\alpha}{2\pi} \int_0^{2\pi} d\varphi \, \cos(\Delta a)(e + \sin e \cos e - e_{\min} - \sin e_{\min} \cos e_{\min}) \qquad (5.19)$$

An approximation for small e is

$$G \approx \frac{\sin\alpha}{\pi} \int_0^{2\pi} d\varphi \, \cos(\Delta a)(\sin e - \sin e_{\min})$$

For comparison, the surface area (in steradian) visible from an inclined surface is

$$\Omega_{\text{land}} = \iint d\Omega = \int_0^{2\pi} \int_{e_{\min}(\varphi)}^{e(\varphi)} de \, d\varphi \cos e = \int_0^{2\pi} d\varphi \left(\sin e - \sin e_{\min}\right)$$

5.5   Outline of Implementation

The algorithm is separated into two parts.

The first, described in section 5.3, determines the horizons and view factors of all surface elements with all other surface elements. This information is written to files `horizons.dat` and `viewfactors.dat`, respectively. This part is easily parallelized, as calculations for each pixel are independent of one another although the entire topography has to be loaded into memory at once. For parallelization, one slice of the spatial domain is run on each CPU core. It can be submitted to a computer cluster as an array job.

In the `horizons` file, each line is preceded by the integer pixel coordinates. The file is rectangular, and the number of entries is (number of azimuth rays + 2)×(number of topographic pixels). The `viewfactors` file is giant and it is not rectangular. Each line in the output file corresponds to a topographic pixel and at the beginning specifies the number of pixels within field of view. Each visible pixel has then three numbers stored with it: The two integer pixel coordinates and the view factor, $d\Omega$, for this pixel. Non-visible pixels are not stored.

Horizons calculations are implemented in `shadows.f90` and its subroutines. If the view factors are desired, use `fieldofviews.f90`. Horizon heights are also calculated within `fieldofviews.f90`, but with a slightly different algorithm than in `shadows.f90`.

The second part, described in section 5.4, simulates the time evolution of illumination and surface temperature as the sun moves through the sky, using the horizons and (optionally) the field of view as input. The horizons are read in a module called `newhorizons`, which also interpolates horizon elevations for any desired azimuth. The field of view information is read with a separate subroutine. To save memory, the pixel coordinates are stored as 2-byte integers and the spherical angles as 4-byte floating point numbers, respectively, half of the common byte lengths.

The surface energy balance is integrated over time at steps of a fraction (e.g., 1/50th) of a solar day. Surface temperature and illumination are updated at every time step, and thus reflection is taken into account to the order of the number of time steps within a solar day, which is large. The time step is explicit, but the subsurface model, if used, is semi-implicit. The names of the main programs start with `cratersQ_*`.

Overview of current implementations:

Main program	Task	Reflections	Parallel
shadows	pre-calculate horizons, optional multigrid	N/A	yes
fieldofviews	pre-calculate view factors, no multigrid	N/A	yes
insol3d_earth	direct insolation only, Mauna Kea atm.	no	no
insol3d_mars	direct insolation only, no atmosphere	no	no
cratersQ_equilbr	equilibrium solution for airless body	yes	no
cratersQ_moon	airless body	yes	no
cratersQ_mars	Mars orbit and atmosphere	G-approx.	no
cratersQ_mars_parallel	Mars orbit and atmosphere	G-approx.	yes
cratersQ_mars_full	Mars orbit and atmosphere	yes	no

The current implementations use the following naming convention. The input topography to `horizons.f90` is *name*`.xyz`, and the output will be `horizons.dat` for the sequential implementation or `horizon.`*arg* for the parallel implementation, where *arg* is an integer. cratersQ_* expects input files *name*`.xyz`, `horizons.`*name*, and optionally `viewfactors.`*name*. File names and their associated parameters are specified in module `filemanager`, that the user edits.

`insol3d_earth` was used in Schorghofer et al. (2017) and Schorghofer (2018), `cratersQ_mars_parallel` in Schorghofer et al. (2019), and `cratersQ_moon` in Hayne et al. (2019).

5.6 Diffuse Irradiance from Atmosphere in the Presence of Horizons

For bodies with atmosphere, the diffuse irradiance from the sky is assumed to be isotropic (Lambertian), both for short-wave and long-wavelength radiation. In the literature more than one definition of (sky) view factor is in use. The sky view factor F is the spherical angle of the visible sky divided by 2π. The size of the sky (between 0 and 2π steradian) can be calculated from either the horizon heights or the view factors of the landscape segments. The alternative is to weigh the diffuse irradiance from the atmosphere with the cosine of the incidence angle. This is the view factor V as defined above for land segments. In the notation of example (d) above, the factor F is to be replaced with $1 - G$ in the next two equations below. See also Rakovec and Zakšek (2012) for discussion.

For Mars, in the spirit of the Kieffer approximation (subsection 1.2.3),

$$Q_{\text{a,IR}} = Q_0 F f_{\text{IR}} \sin \beta_{\text{noon}}, \tag{5.20}$$

and if the sun is up, then

$$Q_{\text{a,scat}} = \frac{1}{2} Q_0 (1 - A) F f_{\text{scat}}, \tag{5.21}$$

otherwise $Q_{\text{a,scat}} = 0$. (For a planar slope $F = 1 - \alpha/2\pi$, so this does not match the approximation chosen in section 5.2, which uses the other version of the sky view factor).

For (high-elevation) regions on Earth (such as Mauna Kea), short-wavelength irradiance scattered or absorbed by the atmosphere is considered, as described in section 4.1.

Bibliography

O. Aharonson and N. Schorghofer. Subsurface ice on Mars with rough topography. *J. Geophys. Res.*, 111(E11):E11007, 2006.

E. S. Flo Heggem, B. Etzelmüller, and I. Berthling. Topographic radiation balance models: sensitivity and application in periglacial geomorphology. *Norsk Geografisk Tidsskrift-Norwegian Journal of Geography*, 55(4):203–211, 2001.

P. O. Hayne, O. Aharonson, and N. Schorghofer. Micro-cold traps on the Moon. 2019. Submitted.

H. H. Kieffer, T. Z. Martin, A. R. Peterfreund, B. M. Jakosky, E. D. Miner, and F. D. Palluconi. Thermal and albedo mapping of Mars during the Viking primary mission. *J. Geophys. Res.*, 82: 4249, 1977.

M. A. Kreslavsky and J. W. Head. Mars at very low obliquity: atmospheric collapse and the fate of volatiles. *Geophys. Res. Lett.*, 32(12):L12202, 2005.

J. Rakovec and K. Zakšek. On the proper analytical expression for the sky-view factor and the diffuse irradiation of a slope for an isotropic sky. *Renewable Energy*, 37(1):440–444, 2012.

N. Schorghofer. Permafrost survey on the Maunakea summit plateau: Final report. Technical report, University of Hawaii, 2018. 28pp.

N. Schorghofer and K. S. Edgett. Seasonal surface frost at low latitudes on Mars. *Icarus*, 180(2): 321–334, 2006.

N. Schorghofer, M. Leopold, and K. Yoshikawa. State of high-altitude permafrost on tropical Maunakea volcano, Hawaii. *Permafrost and Periglacial Processes*, 28:685–697, 2017.

N. Schorghofer, J. S. Levy, and T. A. Goudge. High-resolution thermal environment of recurring slope lineae in Palikir Crater, Mars and its implications for volatiles. *J. Geophys. Res.*, 2019. in press.

A. Spiga and F. Forget. Fast and accurate estimation of solar irradiance on martian slopes. *Geophys. Res. Lett.*, 35:L15201, 2008.

Part 6

Surface-bounded Exospheres

Monte-Carlo Model of Ballistically Hopping Molecules

History: developed 2012–2017
Core routines are implemented in `montecarlo.f90`

6.1   Introduction

The ballistic trajectories of neutral molecules or atoms in a surface-bounded exosphere are simulated with a Monte-Carlo method. Individual water molecules are launched with probabilistically distributed cartesian velocity components that amount to a random initial azimuth and thermal speed appropriate for the local surface temperature. The model then computes the molecule's impact location and time analytically. An event-driven algorithm is used, where landing and launching events are processed in time-order. Events are scheduled and processed until the molecule is destroyed or lost or until its landing or launch time is beyond the next thermal model time step, when surface temperatures are updated.

Each molecule has a longitude $p_r[1]$, latitude $p_r[2]$, status p_s (on surface $=0$, in-flight $=1$, lost or cold-trapped < 0), and time to the next event p_t (until it arrives on the surface or until it will leave the surface). Negative status values can be used to keep track of where the particle is trapped or how it was lost. Surface temperatures are calculated with a 1D thermal model, as in Part 1.

6.2   Ballistic Flight on Sphere

d ... flight distance (measured along surface of sphere)
t ... duration of flight
τ_{res} ... surface residence time
τ_{dissoc} ... photo-destruction time scale
v_{esc} ... escape speed
v_1 ... initial velocity along longitude direction
v_2 ... initial velocity along meridian
v_3 ... initial vertical (radial) velocity component
az ... azimuth
$\Delta\phi$ ... difference in longitude

λ ... latitude
M ... molar mass
R_{moon} ... radius of body

A ballistic molecule moves on a plane that goes through the center of sphere/body; the ground track is thus part of a great circle.

At launch, each of the three velocity components is picked from a Gaussian distribution, which involves a scaling factor of $\sqrt{T_{\text{surf}}8314.5/M}$. This will lead to a Maxwellian velocity distribution and uniformly distributed launch azimuths. Other probability distributions can be implemented, if desired. For example, an Armand distribution may be appropriate for desorbed molecules.

6.2.1 Constant gravity

For constant g,

$$t = 2v_3/g \tag{6.1}$$

$$d = \frac{2}{g}v_3\sqrt{v_1^2 + v_2^2} \tag{6.2}$$

If $|v| > 0.4v_{\text{esc}}$, then use non-uniform gravity formulae (Sec. 6.2.2)
If $|v| > v_{\text{esc}}$, then gravitational escape
The landing latitude and longitude (λ_2, $\phi_1 + \Delta\phi$) are calculated from the starting coordinates (λ_1, ϕ_1) with the following equations:

$$\cos(az) = v_2/\sqrt{v_1^2 + v_2^2} \tag{6.3}$$

$$\sin\lambda_2 = \sin(d/R_{\text{moon}})\cos(\lambda_1)\cos(az) + \sin(\lambda_1)\cos(d/R_{\text{moon}}) \tag{6.4}$$

$$\cos\lambda_2 = \sqrt{1 - \sin^2\lambda_2} \tag{6.5}$$

$$\cos(\Delta\phi) = \frac{\cos(d/R_{\text{moon}})\cos(\lambda_1) - \sin(\lambda_1)\sin(d/R_{\text{moon}})\cos(az)}{\cos\lambda_2} \tag{6.6}$$

Roundoff issues: if $\cos(\Delta\phi) > +1$ then $\cos(\Delta\phi) = +1$; if $\cos(\Delta\phi) < -1$ then $\cos(\Delta\phi) = -1$.

$p_r(2) = \arcsin(\sin\lambda_2)$
$\Delta\phi = \arccos(\cos(\Delta\phi))$
if $v_1 < 0$, then $\Delta\phi = -\Delta\phi$
$p_r(1) = p_r(1) + \Delta\phi$
if $(\cos\lambda_2 == 0)$ then on pole
$p_r(1)$ is normalized to 0...360°.

$p_t = p_t + t$

6.2.2 Non-uniform gravity

Ballistic travel distance d and flight duration t can also be calculated analytically for a radially dependent gravitational acceleration. Radial variations in g are small for typical thermal speeds

on Mercury and on the Moon, but necessary for Ceres and for super-thermal species on the Moon. The following equations are derived from those in Vogel (1966) and Kegerreis et al. (2017).

a ... semi-major axis of ballistic trajectory
e ... eccentricity of ballistic trajectory
α ... zenith angle of launch velocity, $\alpha = \arctan\left(\sqrt{v_1^2 + v_2^2}/v_3\right)$
Instead of (6.1) and (6.2) use

$$\gamma = (|v|/v_{\text{esc}})^2 \tag{6.7}$$

$$a = \frac{R_{\text{moon}}}{2(1-\gamma)} \tag{6.8}$$

$$e = \sqrt{1 - 4\gamma(1-\gamma)\sin^2\alpha} \tag{6.9}$$

$$d = 2R_{\text{moon}}\arccos\left(\frac{1}{e}(1 - 2\gamma\sin^2\alpha)\right) \tag{6.10}$$

$$E_p = 2\arctan\left(\sqrt{\frac{1+e}{1-e}}\tan\frac{d}{4R_{\text{moon}}}\right) \tag{6.11}$$

$$t = \frac{R_{\text{moon}}}{v_{\text{esc}}}\frac{E_p + e\sin E_p}{(1-\gamma)^{3/2}} \tag{6.12}$$

These equations are not suitable for small launch velocities due to roundoff.

Round-off issues:

a) If e is very close to 1 (fast near-horizontal launch), then based on Taylor expansion of (6.10) and (6.11),

$$d = 4\gamma R_{\text{moon}}\sin\alpha \tag{6.13}$$

$$E_p = 2\arctan\sqrt{\frac{\gamma}{1-\gamma}} \tag{6.14}$$

b) If $1 - 2\gamma\sin^2\alpha > e$ (horizontal launch), do something, otherwise $d = \texttt{NaN}$

Then use (6.3)–(6.6) as before.

6.3   Other Model Components

6.3.1   Photo-destruction

Molecules are lost in-flight by photo-destruction (Table 6.1), at a rate of $t/(\tau_{\text{dissoc}}R^2)$, where R is the distance from the sun, often approximated by the semi-major axis. Require incident flux $Q > 0$, since this only occurs on the dayside. A comprehensive compilation of photo-destruction rates can be found in Huebner et al. (1992). A database is maintained at `http://phidrates.space.swri.edu/`.

6.3.2   Coriolis effect

The Coriolis effect is incorporated by adding tangential velocities but subtracting the distance the surface has traveled during time of flight.

	M	τ_{dissoc}	
H₂O	18.015	20×3600	Potter and del Duca (1964)
H₂O		1/12.6e-6	Crovisier (1989), normal sun
H₂O		1/23.0e-6	Crovisier (1989), active sun
He	4.0026	1.9e7	Killen and Ip (1999)
Ar-40	39.96	3.2e6	Killen and Ip (1999)

Table 6.1: Some pertinent parameters. τ_{dissoc} = photodissociation time scale at 1 AU

At launch:
$$v_1 = v_1 - \frac{2\pi R_{\mathrm{moon}}}{\mathrm{siderealDay}} \cos(p_r(2)) \tag{6.15}$$

After landing:
$$p_r(1) = p_r(1) + t/\mathrm{siderealDay} \tag{6.16}$$

The Coriolis effect is negligible on the Moon and on Mercury, but noticeable on Ceres.

6.3.3 Event driver

Process events over the time step of the thermal model Δt_T, e.g., one hour

```
if (pt > ΔtT) exit
case(ps < 0) exit !  not alive
case(ps==0) !  leaving
   hop once, update pt
case(ps==1) !  landing
   if (incoldtrap) then
      pt = ∞
      cycle
   endif
   evaluate τres(Tsurf)
   pt = pt + τres
```

After all events within Δt_T are processed, subtract Δt_T from all times: if $(\mathbf{p_s} >= 0)\ p_t = p_t - \Delta t_T$. (Moving time zero helps avoid truncation errors after a long run.)

6.3.4 Residence times

Temperature also sets the residence time of water molecules on the surface, which is negligible on most of the lunar dayside and very long on most of the lunar nightside. Many older models use a binary choice, where molecules either immediately hop on the day side or reside indefinitely on the surface on the nightside. This model uses a molecular residence time that depends continuously on temperature instead of a threshold temperature.

For crystalline ice, the average molecular surface residence time only depends on temperature T, but for adsorbed water it is also a function of the adsorbate density θ (number of H₂O molecules

per area). The average residence time is given by

$$\tau_{\text{res}} = \frac{\theta_m}{E(T, \theta)} \tag{6.17}$$

where E is the sublimation rate and $\theta_m = 10^{19}$ m^{-2} is the areal number density of an H$_2$O monolayer. A special case of this parametrization is $\tau_{\text{res}} = c\theta_m/E(T)$, where E is the sublimation rate of pure ice. For pure ice $c = 1$. For example, $c = 1/400$ is reasonable for 0.1 monolayers (Schorghofer and Aharonson, 2014). The functional form of $E(T)$ is almost the same as using a vibrational frequency multiplied by a Boltzmann (Arrhenius) factor.

For non-condensible exospheric species, e.g. helium, $\tau_{\text{res}} = 0$.

Discussion: A fraction of particles bounces elastically from the surface rather than accommodating thermally and leaving at a velocity unrelated to the incoming velocity. The fraction is closely related to the "accommodation coefficient" or "condensation coefficient", and it is temperature dependent. The equilibrium vapor pressure is defined as the flux of water molecules from the gas to the condensed phase being equal to the flux in the opposite direction. Elastic (non-condensing) bounces are not directly implemented in the model.

The exosphere model was used in Schorghofer (2014) (with constant g) and Schorghofer et al. (2016, 2017a,b) (with non-uniform gravity).

Bibliography

J. Crovisier. The photodissociation of water in cometary atmospheres. *Astr. & Astrophys.*, 213: 459–464, 1989.

W. F. Huebner, J. J. Keady, and S. P. Lyon. Solar photo rates for planetary atmospheres and atmospheric pollutants. *Astrophysics and Space Science*, 195:1–294, 1992.

J. A. Kegerreis, V. R. Eke, R. J. Massey, S. K. Beaumont, R. C. Elphic, and L. F. Teodoro. Evidence for a localized source of the argon in the lunar exosphere. *J. Geophys. Res.*, 122:2163–2181, 2017.

R. M. Killen and W.-H. Ip. The surface-bounded atmospheres of Mercury and the Moon. *Rev. Geophys.*, 37(3):361–406, 1999.

A. E. Potter and B. del Duca. Lifetime in space of possible parent molecules of cometary radicals. *Icarus*, 3:103, 1964.

N. Schorghofer. Migration calculations for water in the exosphere of the Moon: Dusk-dawn asymmetry, heterogeneous trapping, and D/H fractionation. *Geophys. Res. Lett.*, 41:4888–4893, 2014.

N. Schorghofer and O. Aharonson. The lunar thermal ice pump. *Astrophys. J.*, 788:169, 2014.

N. Schorghofer, E. Mazarico, T. Platz, F. Preusker, S.E. Schröder, C.A. Raymond, and C.T. Russell. The permanently shadowed regions of dwarf planet Ceres. *Geophys. Res. Lett.*, 43:6783–6789, 2016.

N. Schorghofer, S. Byrne, M. E. Landis, E. Mazarico, T. H. Prettyman, B. E. Schmidt, M. N. Villarreal, J. Castillo-Rogez, C. A. Raymond, and C. T. Russell. The putative cerean exosphere. *Astrophys. J.*, 850:85, 2017a.

N. Schorghofer, P. Lucey, and J.-P. Williams. Theoretical time variability of mobile water on the moon and its geographic pattern. *Icarus*, 298:111–116, 2017b.

U. Vogel. Molecular fluxes in the lunar atmosphere. *Planetary and Space Science*, 14:1233–1252, 1966.